

Fabrication of SrTiO₃/g-C₃N₄ heterostructures for visible light-induced photocatalysis

Meiriele Antunes Ferreira^{a,*}, Gelson T.S.T. da Silva^b, Osmando F. Lopes^c,
Valmor R. Mastelaro^d, Caue Ribeiro^{b,e}, Manoel J.M. Pires^{a,f}, Andréa R. Malagutti^g,
Waldir Avansi Jr.^h, Henrique A.J.L. Mourão^{a,f,**}

^a Programa de Pós-graduação em Química, Universidade Federal dos Vales do Jequitinhonha e Mucuri (UFVJM), 39100-000, Diamantina, MG, Brazil

^b Embrapa Instrumentação, 13561-206, São Carlos, SP, Brazil

^c Instituto de Química, Universidade Federal de Uberlândia (UFU), Uberlândia, MG, 38400-902, Brazil

^d Instituto de Física de São Carlos, Universidade de São Paulo (USP), São Carlos, SP, 13566-590, Brazil

^e Forschungszentrum Jülich GmbH, Institute of Energy and Climate Research (IEK-14): Electrochemical Process Engineering, 52425 Jülich, Germany

^f Instituto de Ciência e Tecnologia, Universidade Federal dos Vales do Jequitinhonha e Mucuri (UFVJM), Diamantina, MG, 39100-000, Brazil

^g Departamento de Farmácia, Universidade Federal dos Vales do Jequitinhonha e Mucuri (UFVJM), Diamantina, MG, 39100-000, Brazil

^h Laboratório de Materiais Multifuncionais Nanoestruturados, Departamento de Física, Universidade Federal de São Carlos (UFSCar), Rodovia Washington Luiz, km 235, 13565-905, São Carlos, SP, Brazil

ARTICLE INFO

Keywords:

Strontium titanate
Graphitic carbon nitride
Heterostructure
Visible-light photocatalysis
Organic pollutant

ABSTRACT

We investigated a new method for the preparation of visible light-activated heterostructured photocatalysts made up of SrTiO₃ (STO) and g-C₃N₄ (CN). The photocatalysts were synthesized by the polymeric precursor method to obtain STO, which was further thermally treated at 550 °C for 2 h in presence of melamine at different proportions for CN formation. The SrTiO₃/g-C₃N₄ heterostructures were termed as STOCN-Mel88%, STOCN-Mel92%, STOCN-Mel95%, STOCN-Mel97% and STOCN-Mel99% indicating the use of melamine at 88%, 92%, 95%, 97% or 99%. The SrTiO₃/g-C₃N₄ heterostructures were characterized for their crystalline structure, optical properties, thermal stability, morphology and surface composition, and photocatalytic potential, which was evaluated by photodegradation of methylene blue dye and amiloride under visible light. The melamine content exhibited a strong influence on the formation of CN, as well as on the bulk structure, surface and photocatalytic properties of the SrTiO₃/g-C₃N₄ heterostructures. The heterostructures were catalytically active under visible light due to their reduced band gap energy. The presence of oxygen vacancies in the STO phase associated with the CN phase improved the photogenerated electron-hole charge separation in the SrTiO₃/g-C₃N₄ catalysts. The synthesis described here is efficient in obtaining visible light-activated photocatalysts that are applicable to photocatalytic processes under solar light.

1. Introduction

Strontium titanate (SrTiO₃, STO) has ideally a cubic perovskite-like structure of ABO₃ oxides, in which the Sr²⁺ and Ti⁴⁺ ions form the A- and B-sites, respectively. However, a real perovskite-like STO exhibits lattice distortion at various extents, which influences on the crystal field and, consequently, the dipole and electronic band structures. Such lattice distortion determines the photogenerated charge carrier behavior of STO that is significant for photocatalytic processes such as excitation,

transfer, and redox reactions [1].

STO can be obtained by different methods, typically exhibiting a band gap between 3.2 and 3.4 eV [2,3]. Due to this, high band gap, STO is used in photocatalytic processes based on UV irradiation, limiting its scaled-up applications, since sunlight comprises only a small amount of UV radiation. In this sense, doping STO with elements, such as S, C or N, and II-type heterostructures emerges as an alternative to broad the absorption spectrum of this semiconductor [4–7].

Heterostructured semiconductors are composite materials based on

* Corresponding author.

** Corresponding author. Instituto de Ciência e Tecnologia, Universidade Federal dos Vales do Jequitinhonha e Mucuri (UFVJM), 39100-000, Diamantina-MG, Brazil.

E-mail addresses: meirielealm@gmail.com (M.A. Ferreira), henrique.mourao@ict.ufvjm.edu.br (H.A.J.L. Mourão).

<https://doi.org/10.1016/j.mssp.2019.104887>

Received 3 August 2019; Received in revised form 8 December 2019; Accepted 13 December 2019

Available online 26 December 2019

1369-8001/© 2019 Elsevier Ltd. All rights reserved.

two or more semiconductors. The coupling of semiconductors with desired band levels provides an excellent way to enhance the performance of photocatalysts through reactive oxygen species generation [8]. For visible light photocatalysis, it is expected that at least one semiconductor must be visible-light active. In this context, C_3N_4 (CN) is a promising material for creating visible light-activated heterostructures, since its band gap (about 2.7 eV) is lower than those of several other semiconductors [9–15]. Another exceptional feature of CN is its facile synthesis using cheap and available precursors: CN can be obtained by thermal condensation of nitrogen-rich precursors, such as urea, cyanamide, melamine, among others [16]. Recently, some works have focused on the preparation of CN-based heterostructures, activating these photocatalysts with visible and sunlight due to these advantages [17,18].

The coupling of semiconductors is not trivial, since the conditions necessary to synthesize each component is generally different. Differences in thermal stability could also prevent the association between semiconductors. In addition, a proper interface (heterojunction) between the semiconductive phases is key to enable the charge transfer and improve the heterostructure properties compared to the pure semiconductors. Hence, new studies on the synthesis of visible light-activated photocatalysts will probably contribute for the consolidation of semiconductor-based photocatalysis at large scale [15,19].

In this paper, we describe the synthesis of $SrTiO_3/g-C_3N_4$ photocatalyst heterostructures by thermal treatment of STO, previously obtained by the polymeric precursor method, in presence of different mass amounts of melamine (Mel) as a CN precursor. The principal aim was to couple a visible light-inactive semiconductor photocatalyst (STO) with other semiconductor (CN) that can be activated by visible light.

2. Experimental section

2.1. Synthesis of $SrTiO_3/g-C_3N_4$ heterostructures

STO was synthesized by the polymeric precursor method [20]. Briefly, strontium chloride ($SrCl_2 \cdot 6H_2O$, Aldrich) and titanium isopropoxide ($Ti[OCH(CH_3)_2]_4$, Aldrich) were dissolved separately in aqueous citric acid solution ($C_6H_8O_7$, Aldrich) at an acid:metal molar ratio of 3:1. Then, ethylene glycol ($C_2H_4O_2$, Aldrich) was added to both solutions at a mass proportion of 40:60 (ethylene glycol:acid), yielding the polymeric resins of Sr^{2+} and Ti^{4+} both at 0.10 mol L^{-1} . These resins were further mixed, placed (10 mL) in an alumina crucible and heated at $550 \text{ }^\circ\text{C}$ in a muffle for 2 h to obtain the STO powder. Pure CN was obtained by thermal polycondensation of 5 g melamine (Mel) ($C_3H_6N_6$, Aldrich) at $550 \text{ }^\circ\text{C}$ for 2 h in a conventional furnace in air, yielding approximately 0.845 g (16.9%) of CN.

The $SrTiO_3/g-C_3N_4$ heterostructures were synthesized by the mixture of the as-synthesized STO and Mel with subsequent thermal treatment at $550 \text{ }^\circ\text{C}$ for 2 h. The steps are schematized in Fig. S1. The amounts (in grams) of STO and Mel used in each synthesis are described in Table 1. The samples were termed as STOCN-MelX%: STOCN-Mel88%, STOCN-Mel92%, STOCN-Mel95%, STOCN-Mel97% and STOCN-Mel99% where 88%, 92%, 95%, 97% or 99% are the mass contents of Mel with respect to the total mass (STO plus melamine). Other Mel contents (56% and 86%) were also tested, but the samples were similar to STO and STOCN-

Table 1

Amounts (in grams) of STO and melamine (Mel) used to synthesize $SrTiO_3/g-C_3N_4$ heterostructures.

Samples	m_{STO}	$m_{mel.}$
STO	0.12 g	0 g
STOCN-Mel88%	0.56 g	4.05 g
STOCN-Mel92%	0.37 g	4.05 g
STOCN-Mel95%	0.23 g	4.05 g
STOCN-Mel97%	0.12 g	4.05 g
STOCN-Mel 99%	0.036 g	4.05 g
CN	0 g	5.00 g

Mel88%.

2.2. Characterizations

The thermal decomposition of samples was evaluated by thermogravimetric (TG) analysis in air (Shimadzu TGA-50 equipment) using heating rate of $10 \text{ }^\circ\text{C}/\text{min}$ from $30 \text{ }^\circ\text{C}$ to $700 \text{ }^\circ\text{C}$. Phase purity and crystal structure were determined by X-ray diffraction (XRD) using a Shimadzu – XRD600 equipment using scanning speed of $2^\circ/\text{min}$ in the 2θ range from 5° to 80° (Cu $K\alpha$ radiation and Bragg–Brentano geometry). The diffractograms that indicate crystalline samples were analyzed by Rietveld refinement using the software MAUD [21]. Fourier transform infrared (FTIR) spectra were recorded from 4000 to 400 cm^{-1} using a VARIAN 640-IR FT-IR spectrometer equipped with a ATR accessory. Sample morphology was analyzed by field emission gun scanning electron microscopy (FEG-SEM), using a JEOL JSM-6701F microscope. Transmission electron microscopy (TEM) and Energy Dispersive Spectroscopy (EDS) analysis were conducted on a FEI Tecnai G2 F20 microscope equipped with EDS EDAX and Si detector. X-ray photoelectron spectroscopy (XPS) was carried out using a ScientaOmicron ESCA + equipment with a high-performance hemispheric analyzer (EA 125) with monochromatic Al $K\alpha$ radiation. The operating pressure in the ultra-high-vacuum chamber was 2.10^{-9} mbar. Pass energies of 20 and 50 eV were used for the restricted- and wide-range spectra, respectively. The samples were not submitted to *in situ* heating or Ar^+ sputtering to enable proper determination of light elements, such as C, N and O. The following peaks were used analyzed: O 1s, C 1s, N 1s, Sr 3d and Ti 2p. The C (C, H) component of the C 1s peak of adventitious carbon was assumed at 284.5 eV to set the binding energy scale, and data were treated using the software CasaXPS. Diffuse reflectance spectrometry (DRS) spectra were recorded with a UV–vis spectrophotometer in the range 200–800 nm (Shimadzu UV-2600) equipped with an integrating sphere (ISR-2600 Plus) to determine the band gap of the materials. The band gap energies were estimated using the Tauc plot for the direct allowed transitions obtained from the UV–vis diffuse reflectance spectra data. The band gap energy values were obtained by extrapolation, as described in previous studies [17,22,23]. Specific surface areas (SSA) were calculated according to the BET model using N_2 adsorption data obtained with a Micrometrics ASAP 2000 instrument.

The charge carriers' lifetime of the as-synthesized samples was determined via time-resolved photoluminescence using time-correlated single photon counting (TCSPC). A 405 nm-pulsed laser diode (LDH P-C-405, PicoQuant) with approximate pulse width of 50 ps and 40 MHz repetition rate was used as the excitation source. The PL emission was spectrally resolved using collection optics and an emission monochromator. The TCSPC module (PicoHarp 300, PicoQuant) was used for ultrafast detection.

2.3. Photocatalytic tests

The photocatalytic performance of the samples under visible light irradiation was evaluated in a photoreactor equipped with six fluorescent lamps. Aqueous colloidal sample suspensions were prepared by the dispersion of 10 mg of sample in 20 mL of aqueous solutions of the dye methylene blue (MB) and the drug amiloride (AML), both solutions at 10 mg/L (Fig. S2). The MB and AML concentrations were determined at different periods with a Shimadzu UV 6300 PC Double Beam equipment using wavelengths of 664 nm and 285 nm, respectively. Before the kinetic experiments, the suspensions were kept in the dark for 12 h to achieve the adsorption/desorption equilibrium of the contaminant molecules (MB or AML) on the photocatalyst surface. All measurements were performed in triplicate. The photodegradation curves were linearized using the pseudo-first-order kinetics model to obtain the rate constant of the photodegradation reactions, as described in our previous study [24].

3. Results and discussion

3.1. Characterization of the synthesized materials

Thermogravimetric analysis was performed to investigate the thermal stability and to quantify the g-C₃N₄ phase in the prepared heterostructures. The TG curves showed that the mass loss attributed to the thermal decomposition of pure CN occurred in the range 550–700 °C [25,26]. Taking into account the mass loss observed at low temperatures, attributed to the release of water and hydroxyl groups from the sample surface, it was possible to estimate the g-C₃N₄ content in the heterostructures, as shown in Fig. 1 and Table S1.

The specific surface areas (SSA) are also shown in Table S1. It is possible to note that the presence of melamine during the thermal treatment of STO did not increase the surface area of the heterostructures, since all SSA values of the STOCN_MelX% samples were lower than that of STO. Also, it is possible to observe that the larger the Mel content, the higher the mass loss extent in the thermogravimetric analysis, indicating that the CN content in the STOCN-MelX% samples increase progressively with the increasing Mel percentage. However, the TG curve of the STOCN-Mel88% sample did not show a mass loss related to CN, indicating an insignificant amount of CN in this sample (0% in Table S1). It is worth pointing out that, due to the Mel thermal polycondensation yield (16.9% of CN), a CN content of 55% should be expected for the STOCN-Mel88% sample, as listed in Table S1. The expected CN contents for the other STOCN-MelX% samples are also presented in Table S1.

It is possible to observe that there is a minimum Mel content to enable significant CN formation (88%–92%) using the method described in this study, i.e., mixture of STO with melamine (CN precursor) followed by heating at 550 °C for 2 h. This trend is clearly observed in Fig. 2. The experimental and theoretical CN contents were similar only for the samples obtained from high starting Mel contents, i.e., 97% and 99%.

Fig. 3 shows the diffractograms of STO, CN and STOCN-MelX% (X = 88%, 92%, 95%, 97% and 99%) samples. The XRD pattern of CN shows two broad peaks ascribed to the graphitic carbon nitride (g-C₃N₄) at about $2\theta = 13.2^\circ$ and 27.3° , indexed to the crystallographic planes (100) and (002), respectively (JCPDS n° 87–1526). The first peak corresponds to the in-plane ordering with a repeated distance between the triazine or heptazine units, while the later relates to the planar graphitic interlayer distance of g-C₃N₄ [27]. The cubic perovskite STO phase was identified by the diffraction peaks (110), (111), (200), (211), (220) and (310) (JCPDS Card n° 35–0734). A secondary phase, SrCO₃, was also identified

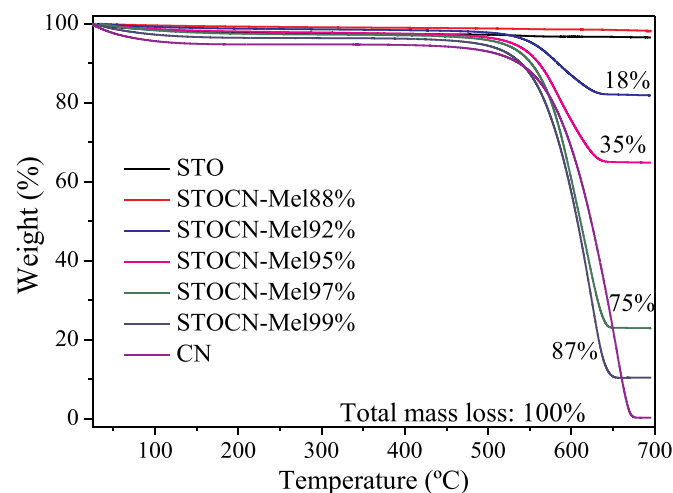


Fig. 1. TG curves of STO, STOCN-Mel88%, STOCN-Mel92%, STOCN-Mel95%, STOCN-Mel97%, STOCN-Mel99% and pure CN.

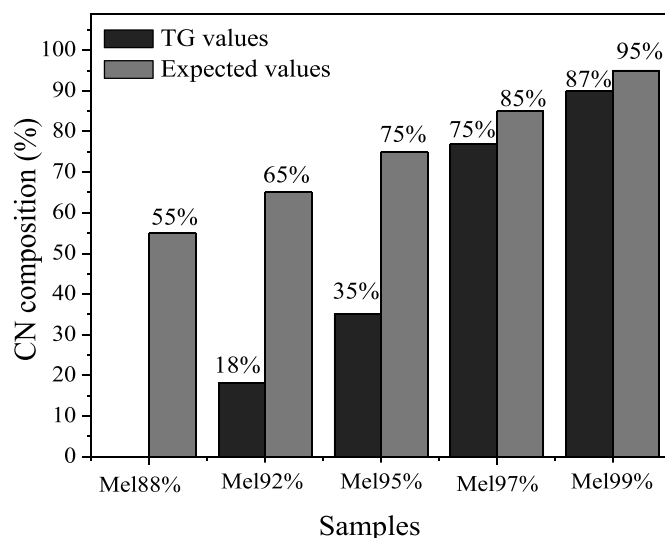


Fig. 2. Comparison of CN contents of STOCN-MelX% samples obtained by TG (experimental - black bars) and calculated from the yield of the pure Mel decomposition (expected (theoretical) - light grey).

by its main diffraction peak at about $2\theta = 25^\circ$ (JCPDS n° 05–0418). SrCO₃ is a usual secondary phase of the STO synthesis, as reported earlier [3,28]. The peaks ascribed to STO observed in the XRD patterns STO and STOCN-MelX% were well-defined, which indicates a high crystallinity for these samples. Also, the intensity of these peaks decreases with the increasing Mel content (and consequently CN content). On the other hand, the main diffraction peak ascribed to the g-C₃N₄ phase indicates its low crystallinity in the samples. The increase of the Mel content progressively increased the CN content in the STOCN-MelX% (92%, 95%, 97% and 99%) samples. However, the peak of CN was not observed in the XRD pattern of STOCN-Mel88%, suggesting that this phase may not be formed from the lowest Mel percentage, as already indicated by TG analysis.

Rietveld refinement was applied to analyze all diffractograms except that of pure CN due to its low crystallinity. Since the peaks of g-C₃N₄ and SrCO₃ are predominant in the low 2θ range, the refinement was restricted to $2\theta \geq 30^\circ$. The Inorganic Crystal Structure Database (ICSD)

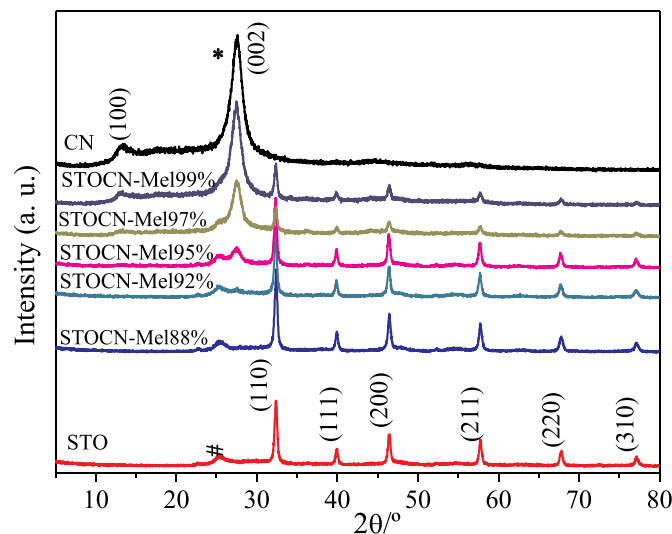


Fig. 3. XRD patterns of STO, STOCN-Mel88%, STOCN-Mel92%, STOCN-Mel95%, STOCN-Mel97%, STOCN-Mel99%, and pure CN. The peaks identified by hkl relate to STO and the symbols # and * correspond to the main peak of the SrCO₃ and g-C₃N₄ phases, respectively.

CIF patterns 23076 and 15195 were used for STO and SrCO₃, respectively. For g-C₃N₄, a CIF file was constructed considering the data furnished by Wang et al. [6] for the g-C₃N₄ phase with P6₃cm hexagonal structure. Data fitting is presented in the supplementary material (Fig. S3). The mean STO crystallite size of the different samples were similar, from 32 to 45 nm, indicating no correlation between the Mel content and the crystallite sizes. The STO lattice parameter was between 3.907 and 3.911 Å, which is very close to the ICSD standard value (3.905 Å).

The main purpose of the Rietveld refinement was to obtain the occupancy fraction of the oxygen sites in the STO structure. The results are presented in Fig. 4. Previous studies used Rietveld refinement to estimate oxygen occupancy [29,30]. As shown in Fig. 4, the oxygen occupancy in STO decreased with the increasing melamine content (Mel %). The tendency in Fig. 4 is clear although the uncertainties are relatively high mainly due to the presence of the little crystalline g-C₃N₄ and SrCO₃ phases.

FTIR spectra obtained in ATR mode are shown in Fig. 5. It is possible to observe clearly that the spectra of STOCN-Mel97% and STOCN-Mel99% were similar to that of pure CN, indicating high amounts of CN in these samples, as already suggested by TG and XRD. A similar indication is seen in the ATR-FTIR spectrum of STOCN-Mel95%. The bands corresponding to the C-N (~1240 cm⁻¹), C=N (~1640 cm⁻¹) and s-triazine ring vibrations (~810 cm⁻¹) were observed [26,31]. It was also observed a broad vibration band at around 3100 cm⁻¹ corresponding to the secondary (NH₂) [26], and primary (N-H) amine stretching [26,31], probably related to the endpoints of the g-C₃N₄ structure. This band is overlapped with the O-H stretching vibration band (3600–3000 cm⁻¹) [32], which indicates a high concentration of hydroxyl groups in the samples comprising high CN contents, albeit it is difficult to separate these signals (NH, NH₂ or OH). On the other hand, the STOCN-Mel88% e STOCN-Mel92% samples presented spectra more similar to that of STO, indicating the higher amounts of STO in these samples. In this way, the main vibrational observation is the band between 500 and 700 cm⁻¹ (maximum at about 540 cm⁻¹) corresponding to the Ti-O stretching vibration [31]. Additionally, the peak related to atmospheric CO₂ (~2350 cm⁻¹) [33] was observed in all spectra, as well as the signal ascribed to carbonate (at about 1470 cm⁻¹) from SrCO₃, especially in the FTIR spectra of STO and STOCN-Mel88% [34].

A previous report on the synthesis of other metal oxide have also shown that there is a minimum Mel content required to obtain significant amounts of CN [24]. However, the results obtained here for the STOCN-MelX% series seem not to be completely clear. A hypothetical explanation is based on the Mel condensation. As previously reported [9, 35], the formation of g-C₃N₄ occurs by polycondensation of the melamine units (triazine units) with release of gaseous NH₃, yielding two- and three-dimensional C₃N₄ structures. Therefore, it is expected that the

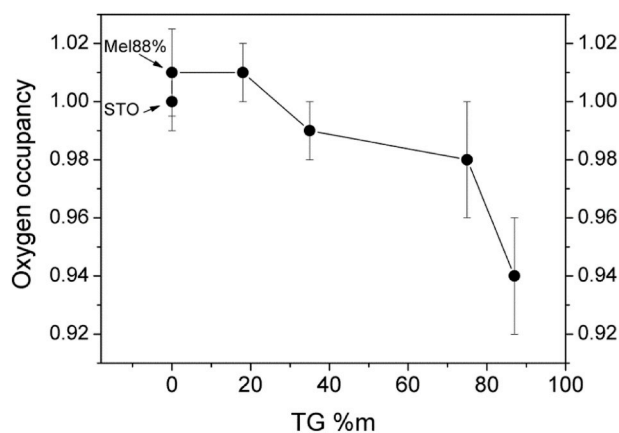


Fig. 4. Oxygen occupancy in STO obtained by Rietveld refinement as a function of the CN content determined by TG analysis.

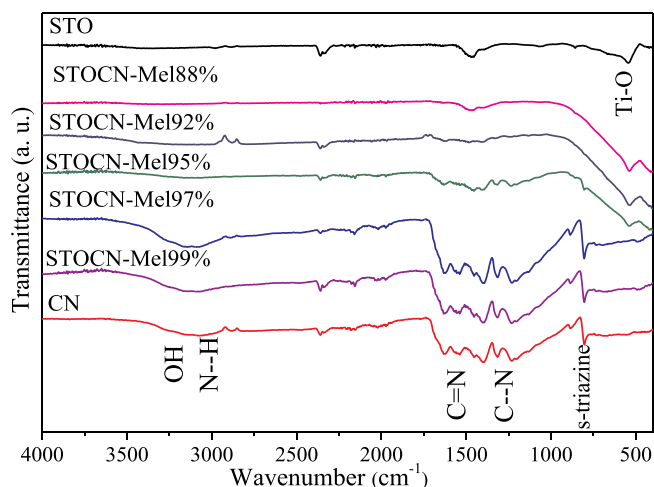


Fig. 5. ATR-FTIR spectra of pure STO, STOCN-Mel88%, STOCN-Mel92%, STOCN-Mel95%, STOCN-Mel97%, STOCN-Mel99%, and pure CN.

greater the Mel concentration, the larger the structure obtained after polycondensation, allowing the formation of the graphitic carbon nitride structure, g-C₃N₄. The dispersion of the Mel molecules in the STO could reduce the polycondensation at a certain extent, thereby hampering the formation of g-C₃N₄. As can be seen in Table 1, the same Mel mass (4.05 g) was used in the synthesis of the STOCN-MelX% heterostructures (88%, 92%, 95%, 97% and 99%). The synthesis conducted with high Mel contents probably ensured a minor dispersion (separation between Mel molecules) of Mel in the STO, which favored the contact between Mel molecules and, consequently, increased the polycondensation extent.

This behavior suggests that the synthesis approach described here is suitable to obtain SrTiO₃/g-C₃N₄ heterostructures, especially when high starting Mel percentage are used to result in large g-C₃N₄ contents (Figs. 1 and 2 and Table S1). The SrTiO₃/g-C₃N₄ heterostructures could be advantageous in visible light-activated photocatalysis, since the yield of the visible light-active catalyst (g-C₃N₄) is optimized.

Fig. 6 shows representative FEG-SEM images of CN, STO, STOCN-Mel92% and STOCN-Mel99%. The samples submitted to thermal treatment are composed of micrometric agglomerates, as expected. Also, it is possible to observe that the morphologies of STOCN-Mel92% (Fig. 6c) and STO (Fig. 6b) were similar, presenting agglomerates probably composed of small STO nanoparticles. This is in accordance with the other results, since both samples presented high STO contents. The morphologies of CN and STOCN-Mel99% (sample with highest g-C₃N₄ content) were also quite similar. These samples are composed of agglomerates with no defined morphology.

Additionally, the STOCN-Mel95% heterostructure was studied by TEM (Fig. 7). From Fig. 7a, it was seen that the sample was composed of two different morphologies, evidenced by image contrast, where a small number of nanoparticles appeared distributed onto particles having lamellar morphology. Indeed, representative EDS analysis confirmed that the lamellar particles were related to the g-C₃N₄ phase, since only peaks related to C and N were observed in the EDS spectrum (Fig. S4a). For the nanoparticles observed in Fig. 7a, the EDS spectrum showed peaks related to the Sr, Ti and O elements (Fig. S4b). Other peaks observed in the spectrum are related to the grid and EDS detector. As a matter of fact, the HRTEM images in Fig. 7b shows that these nanoparticles have a lattice parameter of about 0.28 nm, which was consistent with the (110) interplanar distance of the cubic perovskite STO phase, in good agreement with the XRD results.

Due to the importance of surface properties for photocatalytic processes, XPS was employed to analyze the surface composition and chemical state of the representative samples STOCN-Mel 99%, STOCN-

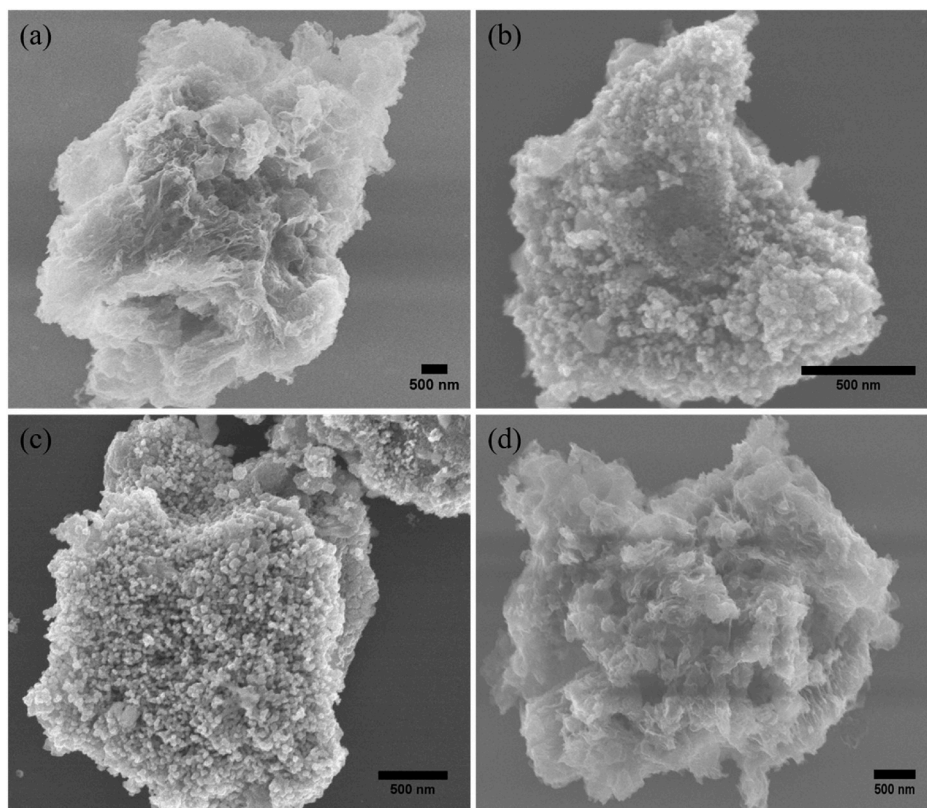


Fig. 6. Representative FEG-SEM images of CN (a), STO (b), STOCN-Mel92% (c) and STOCN-Mel99% (d).

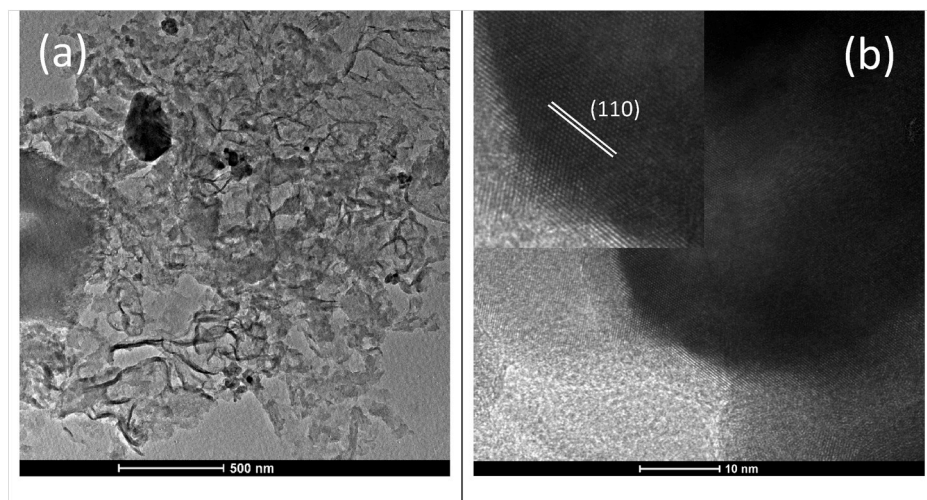


Fig. 7. (a) and (b): TEM images of STOCN-Mel95%. Inset of (b): an expanded view of HRTEM image for a representative SrTiO_3 particle.

Mel 88%, STO and CN. First, the surface atomic percentages were determined from the wide range XPS spectra (Fig. S5) using the Shirley background for all signals in the quantification procedure [36], Table 2. The surface compositions of CN and STOCN-Mel99% were very similar, as well as those between STO and STOCN-Mel88%. Although the percentages of Sr and Ti detected in STOCN-Mel99% were in the uncertainty range, these elements were unequivocally detected in this sample. A similar trend was found in relation to the detection of N in STOCN-Mel88%.

To identify the chemical states of each element, the restricted-range XPS spectra were analyzed in detail. Fig. 8 presents the measurements for C, N and O 1s (for Sr and Ti, see Fig. S6). Once more, it can be noted

Table 2
Surface atomic percentage of CN, STO, STOCN-Mel99% and STOCN-Mel88% determined by XPS.

Samples	Surface atomic percentage (%)				
	C	O	N	Ti	Sr
CN	58.8	5.8	35.4	–	–
STO	44.0	38.0	–	9.6	8.4
STOCN-Mel99%	57.0	7.2	35.2	0.4	0.2
STOCN-Mel88%	36.5	39.7	1.0	10.6	12.2

the similarities between CN and STOCN-Mel99%, and between STO and STOCN-Mel88%. The energies corresponding to the main peaks were very similar, but their intensities varied significantly. The peaks of STO presented a larger width for all elements, which is probably due to the larger SrCO_3 content in this sample rather than that in STOCN-Mel88%.

The restricted-range XPS spectra were fitted using Voigt functions with 30% of Lorentzian contribution. The number of signals in each peak was chosen with basis on the results from the other techniques presented above and peaks clearly observed in each case. The identification of the chemical states was based on previous studies [37–42]. Representative

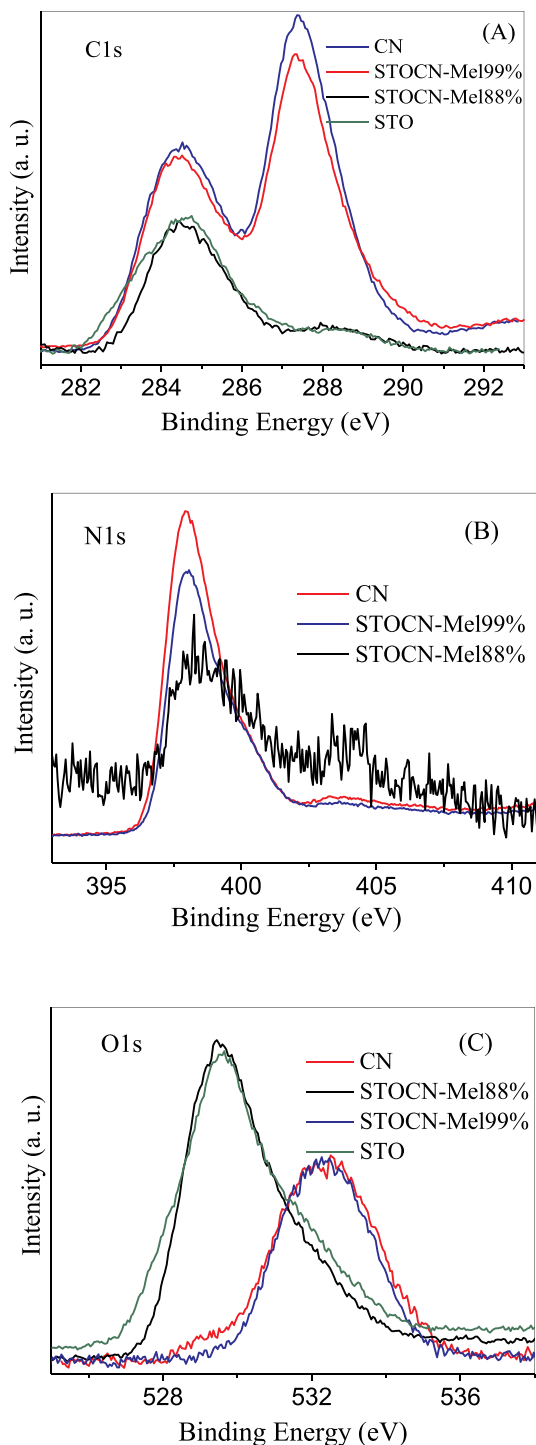


Fig. 8. Comparison of C 1s (A), N 1s (B) and O 1s (C) XPS spectra of CN, STOCN-Mel99%, STOCN-Mel88% and STO.

results are displayed in Fig. 9. The other results are included in the supplementary material (Fig. S6 and Fig. S7). Table S2 presents a detailed atomic composition of possible chemical species and their relative percentages.

For C 1s, good-quality fits were obtained with 3 signals for CN, STOCN-Mel99% and STOCN-Mel88%, and 2 signals for STO. The results of CN presented in Fig. 8 (A) reveals that the most intense signal occurred at 287.3 eV, an energy that corresponds to amino groups from C bonded to 2 or 3 N atoms. This signal can be attributed to C atoms in the g- C_3N_4 structure: the signal intensity in the STOCN-Mel99% spectrum was high as in the spectrum of CN, but it was much less intense in the STOCN-Mel88% spectrum, indicating a minor and null amount of g- C_3N_4 in this sample and STO, respectively. The signal at 284.5 eV relates to adventitious carbon and/or hydrocarbon $\{(\text{CH})_n\}$, and the minority signal at 288.4 eV were attributed to C atoms directly bonded to O atoms

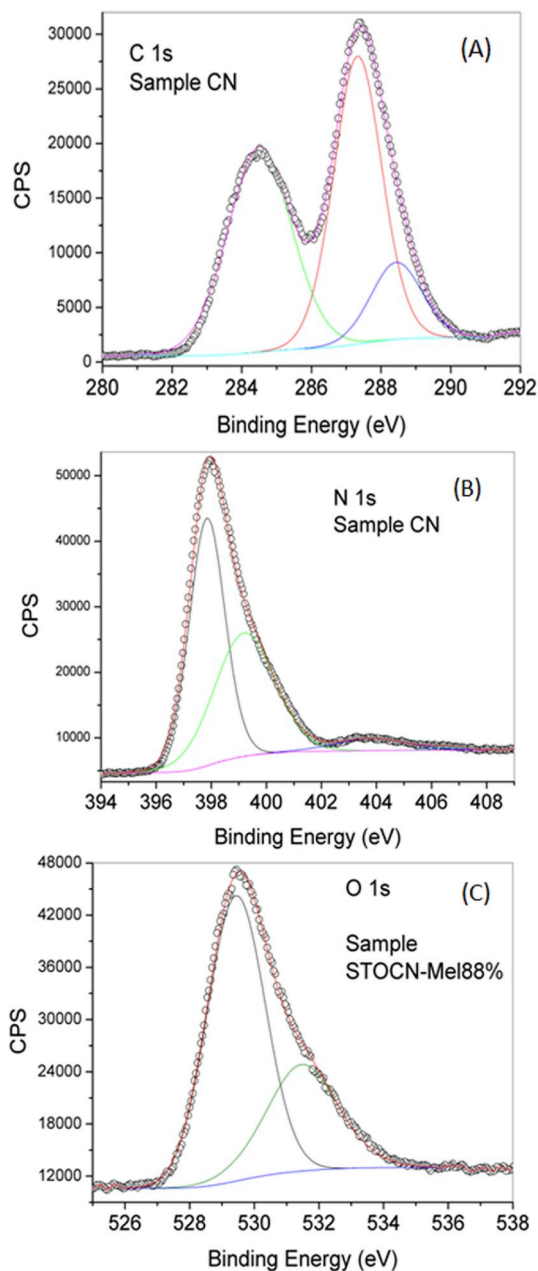


Fig. 9. XPS spectra of peak-fitted C 1s signal for CN (A), peak-fitted N 1s signal for CN (B) and peak-fitted O 1s signal for STOCN-Mel88% (C). The curves for each contribution and the Shirley backgrounds are also presented.

in C–N–O-like bonds. For the STO and STO-CN-Mel88% samples, the C 1s signal appeared at higher energy, 288.1 and 288.2 eV, respectively, which is probably ascribed to SrCO₃, since a significant amount of this phase was detected by XRD.

Concerning the N 1s XPS spectra, 4 signals were used to fit the CN and STO-CN-Mel99% spectra, while 3 signals were used in the case of the STO-CN-Mel88% spectrum. As can be seen in Fig. 8B, the signal to noise ratio in the STO-CN-Mel88% spectrum is poor, then the discussion was focused on the other samples. The fitted CN spectrum is presented in Fig. 9 (B). The main signals at 397.9 eV and 399.3 eV can be attributed to N with double bond with C (N=C) and to N with one (C–N) or more single bonds with C, respectively. The occurrence of these two signals is a common feature of amino groups from g-C₃N₄ [37,39]. The minority signals at 403.8 eV and 406.6 eV can be attributed to N atoms bonded to O atoms, and to π -excitation, respectively. The low intensity and overlap hinder the clear identification of these two signals. The occurrence of π -excitation was expected since a major signal was associated with N with double bond, and the presence of the additional peak at 403.8 eV is inferred due to its relative intensity to π -excitation. The presence of N bonded to O could indicate that the g-C₃N₄ structure endpoints suffered oxidation at a low extent during the thermal treatment in air. This signal is identified in Table S2 as a pyridine-like N–O bond. Considering the C 1s and N 1s signals ascribed to g-C₃N₄ in the CN and STO-CN-Mel99% spectra, the C/N atomic ratios were 0.79 and 0.77, respectively. These values were similar to that of the perfect g-C₃N₄ stoichiometry (0.75), albeit their XRD patterns indicated the presence of g-C₃N₄ with a low crystallinity degree.

A representative fit of the O 1s signal is presented in Fig. 9 (C) for STO-CN-Mel88%. In opposition to CN and STO-CN-Mel99%, the STO-CN-Mel88% sample did not show the signal at 533 eV, which is normally associated with the presence of water. The same result was observed for STO. The two signals in the fitted curve can be ascribed to SrTiO₃ (529.4 eV) and SrCO₃ (531.5 eV). This last signal is a broad peak probably associated with the overlapped additional signals of O bonded to N or C

in a compound other than SrCO₃, although the contribution of SrCO₃ is the predominant one.

The Ti 2p signal was fitted considering only one signal, which is naturally attributed to the SrTiO₃ phase unequivocally detected by XRD. The energies measured for the Ti 2p_{3/2} and 2p_{1/2} peaks also corresponded to the expected Ti values in STO. Considering the atomic percentages of the Ti and O signals associated with STO, the Ti/O ratios obtained for STO-CN-Mel88% and STO were 0.39 and 0.32, respectively. For a perfect stoichiometry, the expected Ti/O ratio is 0.33, thus the XPS results indicate a decrease in the oxygen occupancy in the STO-CN-Mel88% sample compared to STO. The oxygen occupancy in STO-CN-Mel88% is significantly smaller than that observed by XRD, which may be explained by the fact that XPS is a surface-limited technique while XRD assesses mainly the material bulk features. The Ti/O ratio of 0.39 corresponds to an oxygen occupancy of about 0.85, which is small but still in the range tolerated by the perovskite-like STO structure [43]. Thus, both XRD and XPS indicated that the oxygen vacancies increased with the increasing Mel percentage. Indeed, this result confirms the formation of an interface between the STO and CN phases due to the thermal treatment, as already suggested by TEM.

3.2. Photocatalytic performance under visible light irradiation

The photocatalytic potential of the samples was evaluated for the photodegradation of MB and AML (emerging pollutant) triggered by visible light irradiation. Fig. 10 exhibits the photocatalytic degradation curves of these molecules using all samples synthesized in this work. The reaction rate constants (k) were calculated using the pseudo-first-order model, as shown in Fig. S8 and Table 3. The approximated band gap energy values of all samples are also summarized in Table 3. The band gap energy was estimated from the x-axis intercept of the tangent lines of each curve.

It is possible to observe that the direct photolysis of either MB or AML was insignificant, mainly for MB. Also, all photocatalysts were active in

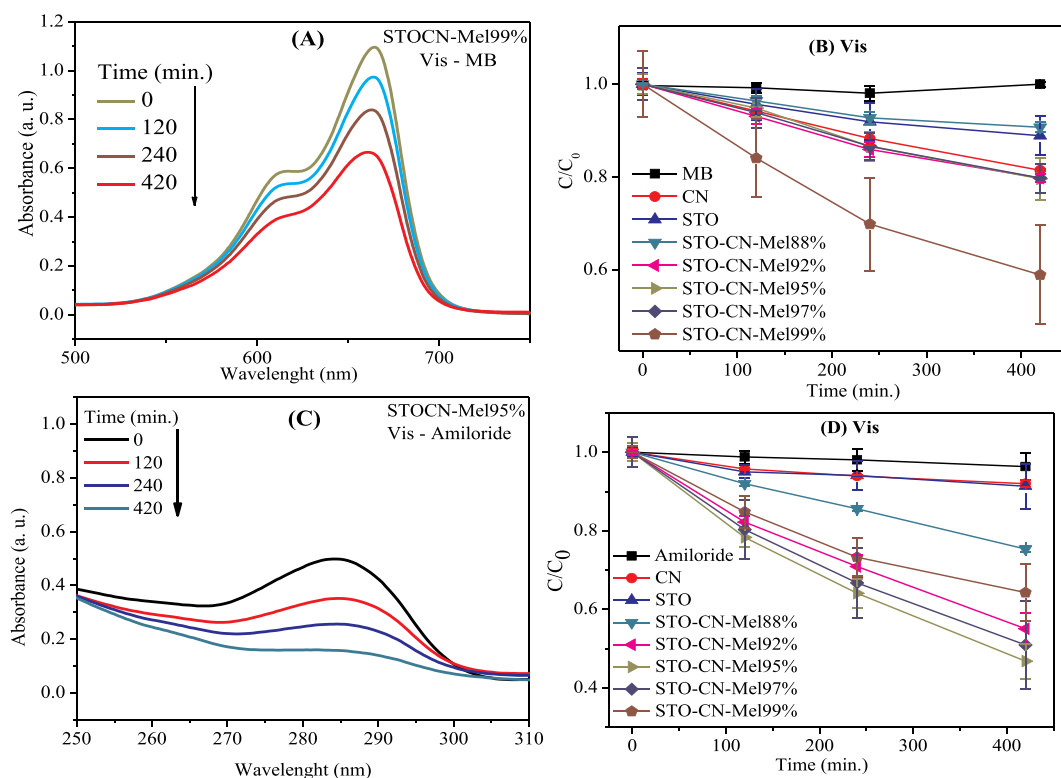


Fig. 10. UV–vis spectra of MB (A) and AML (C) at different times of visible light irradiation in presence of STO-CN-Mel99% and STO-CN-Mel95%, respectively; MB (B) and AML (D) photodegradation curves for all synthesized samples.

Table 3

First-order rate constants (k) for MB and AML visible light-triggered photodegradation and approximate band gap values of all synthesized samples.

Samples	MB $k \times 10^{-3}$ (min. ⁻¹)	R ²	AML $k \times 10^{-3}$ (min. ⁻¹)	R ²	Band gap (eV)
MB	0.00	–	–	–	–
AML	–	–	0.0890	0.9871	–
CN	0.485	0.9977	0.167	0.8783	2.7
STO	0.293	0.9598	0.275	0.8569	3.3
STO-CN-Mel88%	0.250	0.9316	0.666	0.9986	3.2
STO-CN-Mel92%	0.520	0.9830	1.47	0.9966	2.9
STO-CN-Mel95%	0.561	0.9840	1.82	0.9978	2.7
STO-CN-Mel97%	0.545	0.9916	1.64	0.9967	2.8
STO-CN-Mel99%	1.30	0.9795	1.17	0.9647	2.8

the degradation of MB and AML, but their efficiencies were quite different from one another. One important effect for the photocatalytic performance was the decrease in the band gap energy of the STOCN-MelX% samples with the increasing g-C₃N₄ content. This enabled the photoactivation of the photocatalysts through visible light absorption, which was the main goal of this study. As can be seen in Table 3 and Fig. 11, the STOCN-Mel88% sample presented an absorption spectrum and band gap energy similar to those of STO. This result is consistent, since STOCN-Mel88% has a minor amount of g-C₃N₄ that could be detected only by XPS. The STOCN-Mel92% sample presented intermediate band gap value (2.9 eV) and the samples (STOCN-MelX%) having higher g-C₃N₄ contents presented band gap values similar to that of CN (2.7 or 2.8 eV).

The best photocatalytic performances in the MB and AML photodegradations were observed for STO-CN-Mel99% ($k = 1.30 \times 10^{-3}$ /min) and STOCN-Mel95% ($k = 1.82 \times 10^{-3}$ /min), respectively. The STO-CN-Mel99% sample reduced the MB absorption by 40% after 420 min of visible light irradiation, while the STOCN-Mel95% sample removed almost 55% of AML.

For the AML photodegradation, it was clearly observed that all SrTiO₃/g-C₃N₄ heterostructures were more photoactive than STO and CN, including the sample with the lowest g-C₃N₄ content (STOCN-Mel88%). In particular, the k value for STOCN-Mel95% was 6- and 10-fold higher than those for CN and STO, respectively. Indeed, this synergistic effect proved that the coupling between CN and STO as a

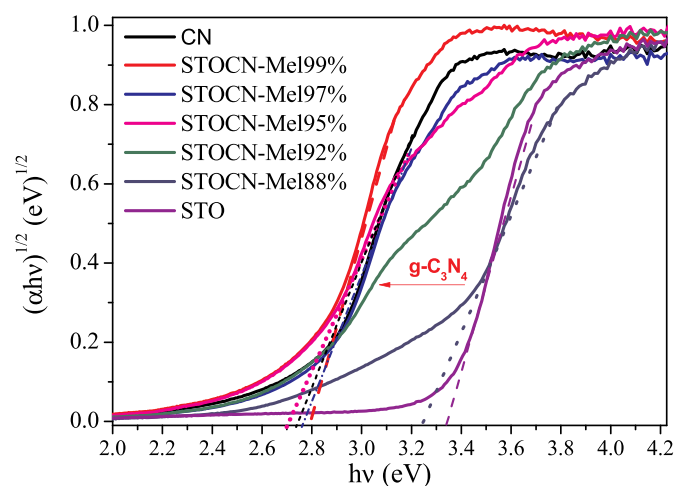


Fig. 11. Tauc plot for direct allowed transition of STO, STOCN-Mel88%, STOCN-Mel92%, STOCN-Mel95%, STOCN-Mel97%, STOCN-Mel99%, and CN obtained from UV-vis diffuse reflectance spectra data.

heterostructure resulted in photocatalysts with enhanced photocatalytic activity.

The constant electron/hole pair (τ) lifetime for STOCN-Mel99% and CN were obtained through time-resolved photoluminescence analysis to confirm the heterojunction formation and consequent increase in the charge carrier lifetime. The measurement was not performed on STO, because of its band gap of 3.3 eV (Fig. 11) which is not low enough to allow activation by laser excitation at 405 nm. Fig. 12 exhibits the decay of PL intensity monitored at 545 nm and excited by a laser source centered at 405 nm for both samples. The PL decays of the samples were fitted with a second-order exponential function to calculate the electron/hole pair lifetime [17]. The PL lifetime of the band-band emission (i.e., the electron/hole pair recombination) for the STOCN-Mel99% heterostructure was 2.15 ns, while that of CN was approximately 0.29 ns, i.e. the composite material presented a constant lifetime approximately 7-fold longer than that of pure g-C₃N₄. These results agree with the results from the photodegradation experiments, confirming that the coupling between SrTiO₃ and g-C₃N₄ formed a suitable II-type heterostructure. This kind of heterostructure provides a spatial separation of the electron/hole pair driven by the difference between the BC and BV reduction potentials of the semiconductor. This effect was crucial to increase the photoactivity of the heterostructures, especially because their SSA were lower than that of STO (Table S1).

Fig. 13 displays a scheme of the proposed photodegradation mechanism of MB and AML in presence of the SrTiO₃/g-C₃N₄ heterostructures. Only the g-C₃N₄ phase is visible light-active, forming holes (h^+) and electrons (e^-) in its valence band (VB) and conduction band (CB), respectively.

In the heterostructures with significant g-C₃N₄ content, the electrons move towards the STO phase, favoring the photogenerated electron-hole pairs separation, which further increases the heterostructure's photocatalytic activity due to the reduced charge recombination. Although the electrons at the CB of STO could also contribute to the formation of radicals, the main way by which the degradation of MB and AML occurs is related to the hole generated at the g-C₃N₄ phase. The hole from the VB of g-C₃N₄ can either directly oxidize the MB (or AML) molecule that are adsorbed onto the photocatalyst surface, or oxidize the adsorbed hydroxyl groups forming hydroxyl radicals (\bullet OH), which further reacts with the MB (or AML) molecule, thereby leading to its decomposition. Both processes can also occur simultaneously, but the latter is the most important for the photocatalytic degradation.

For the SrTiO₃/g-C₃N₄ heterostructures, the former process (direct

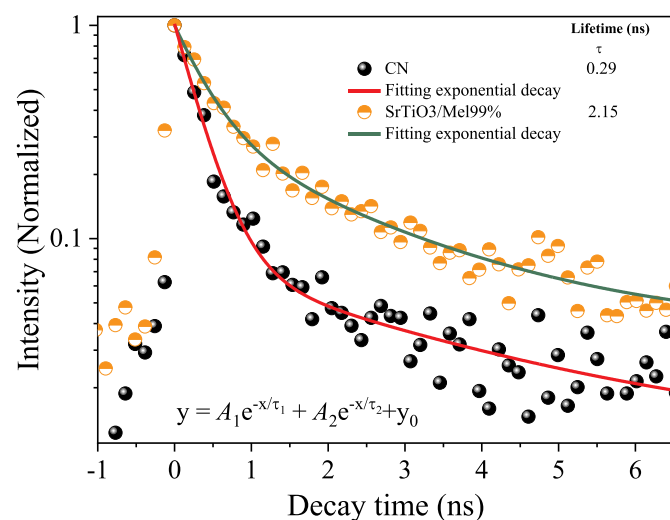


Fig. 12. Time-resolved fluorescence decay spectra of CN and the STOCN-Mel99% excited by laser irradiation at 405 nm and monitored at 544 nm. The solid lines represent the fitted model.

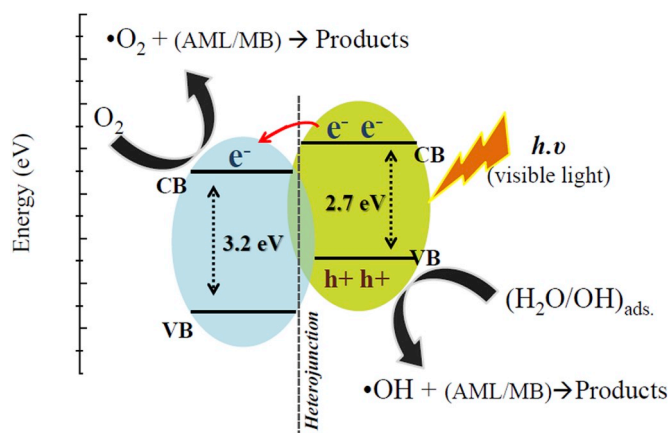


Fig. 13. Schematic illustration of the increased photocatalytic activity and improved charge separation of SrTiO₃/g-C₃N₄ heterostructures activated by visible light.

oxidation of adsorbed molecules) was probably more pronounced for the heterostructures having large g-C₃N₄ content, and mainly for the MB photodegradation, since the adsorption of MB onto the photocatalyst surface was high, as indicate in Fig. S9. Accordingly, the STOCN-Mel99% sample was the most active photocatalyst on the MB degradation: this heterostructure presented the highest amount of g-C₃N₄, which increases the absorption of visible light and the adsorption of MB molecules, albeit its minor STO amount makes the charge separation effect less intense.

On the other hand, the adsorption contribution was probably less significant than the charge separation effect in the AML photodegradation. In this case, the STOCN-Mel95% heterostructure exhibited the best performance, since it showed optimized photocatalytic properties, that is, increased visible light absorption and better charge separation.

Furthermore, it is known that the oxygen vacancies can act either as an active adsorption sites in heterogeneous catalysis with pure metal oxides or as a trap for photoelectrons, improving the photogenerated electron-hole pairs separation [44,45]. Thus, the presence of oxygen vacancies at the bulk (XRD) and surface (XPS) of the SrTiO₃/g-C₃N₄ heterostructures could also have favored the photocatalytic degradation of MB and AML.

In conclusion, the SrTiO₃/g-C₃N₄ heterostructures synthesized in this work can be efficiently applied to degrade emerging pollutants using visible light or even sunlight without requiring special lamps. This outcome will make the semiconductor-based photocatalysis cost-effective for visible light-triggered photocatalysts at large scale in sewage treatment plants, among other applications.

4. Conclusions

SrTiO₃/g-C₃N₄ heterostructures with significant photoactivity under visible light were successfully prepared by thermal treatment. The initial melamine content played a crucial role on the photoactivity of the catalysts, since there is a minor content that enables proper formation of g-C₃N₄ in the heterostructures. It was observed that the g-C₃N₄ yield increased with the increasing melamine percentage. For MB photodegradation, the best photocatalytic activity was observed for the SrTiO₃/g-C₃N₄ heterostructure synthesized from the highest melamine percentage (g-C₃N₄ content) (STOCN-Mel99%), whereas the heterostructure obtained with 95% of melamine (STOCN-Mel95%) exhibited the best performance on the AML photodegradation. Changes in the band gap energy, the adsorption of MB (or AML) on the photocatalyst surface and the enhanced separation of photogenerated charges determined the photoactivity of the heterostructures. The STO phase

displayed oxygen vacancies, which probably also favored the charge separation in the heterostructures.

Declaration of competing interest

We declare that the article is original, the article has been written by the stated authors who are ALL aware of its content and approve its submission, the article has not been published previously, the article is not under consideration for publication elsewhere, no conflict of interest exists, or if such conflict exists, and if accepted, the article will not be published elsewhere in the same form, in any language, without the written consent of the publisher.

CRediT authorship contribution statement

Meiriele Antunes Ferreira: Conceptualization, Methodology, Investigation, Writing - original draft. **Gelson T.S.T. da Silva:** Conceptualization, Methodology, Investigation, Writing - original draft. **Osmando F. Lopes:** Conceptualization, Methodology, Investigation, Writing - original draft. **Valmor R. Mastelaro:** Conceptualization, Methodology, Investigation. **Caue Ribeiro:** Conceptualization, Supervision. **Manoel J.M. Pires:** Conceptualization, Investigation, Writing - original draft. **Andréa R. Malagutti:** Supervision, Conceptualization. **Waldir Avansi:** Writing - original draft, Investigation, Methodology, Conceptualization. **Henrique A.J.L. Mourão:** Conceptualization, Methodology, Writing - original draft, Supervision, Project administration.

Acknowledgements

The authors are grateful to CNPq (grant #454438/2014-1, #159866/2018-9, 407497/2018-8 and 311463/2017-7), FAPESP (grant #13/07296-2, 13/07296-2 and #18/01258-5), CAPES (Finance Code 001), and Embrapa Rede AgroNano for the financial support. The authors also thank the support from LMMA sponsored by FAPEMIG (CEX-112-10), SECTES/MG and RQ-MG (FAPEMIG: CEX-RED-00010-14). C.R. also acknowledges Chinese Academy of Sciences (CAS) President's International Fellowship Initiative (PIFI) by financial support and CAPES/Alexander von Humboldt Foundation by Experienced Research Fellowship (CAPES Finance Code 001; CAPES Process 88881.145566/2017-1).

Appendix A. Supplementary data

Supplementary data to this article can be found online at <https://doi.org/10.1016/j.mssp.2019.104887>.

References

- [1] J. Shi, L. Guo, ABO₃-based photocatalysts for water splitting, *Prog. Nat. Sci.: Mater. Inter.* 22 (6) (2012) 592–615.
- [2] A.E. Souza, G.T.A. Santos, B.C. Barra, W.D. Macedo Jr., S.R. Teixeira, C.M. Santos, A.M.O.R. Senos, L. Amaral, E. Longo, Photoluminescence of SrTiO₃: influence of particle size and morphology, *Cryst. Growth Des.* 12 (2012) 5671–5679.
- [3] Henrique A.J.L. Mourão, Osmando F. Lopes, Waldir Avansi Jr., J. Manoel, M. Pires, Solange Souza, Cauê Ribeiro, Valmor R. Mastelaro, SrTi_{1-x}Fe_xO₃ samples obtained by hydrothermal method: the effect of the amount of Fe on structural and photocatalytic properties, *Mater. Sci. Semicond. Process.* 68 (2017) 140–146.
- [4] Katsuya Iwashina, Akihiko Kudo, Rh-doped SrTiO₃ photocatalyst electrode showing cathodic photocurrent for water splitting under visible-light irradiation, *J. Am. Chem. Soc.* 133 (2011) 13272–13275.
- [5] Tina Setinca, Matjaz Spreitzer, Damjan Vengust, Ivan Jerman, Danilo Suvorov, Inherent defects in sol-precipitation/hydrothermally derived SrTiO₃ nanopowders, *Ceram. Int.* 39 (2013) 6727–6734.
- [6] P. Wang, H. Tang, Y. Ao, C. Wang, J. Hou, J. Oian, Y. Li, In-situ growth of Ag₃VO₄ nanoparticles onto BiOCl nanosheet to form a heterojunction photocatalyst with enhanced performance under visible light irradiation, *J. Alloy. Comp.* 688 (2016) 1–7. Part B.
- [7] C. YU, W. Zhou, J.C. Yu, H. Liu, L. Wei, Design and fabrication of heterojunction photocatalysts for energy conversion and pollutant degradation, *Chin. J. Catal.* 35 (10) (2014) 1609–1618.

- [8] Yun Zheng, Zihao Yu, Honghui Ou, Abdullah M. Asiri, Yilin Chen, Xinchun Wang, Black phosphorus and polymeric carbon nitride heterostructure for photoinduced molecular oxygen activation, *Adv. Funct. Mater.* 28 (1–9) (2018) 1705407.
- [9] J. Wen, J. Xie, X. Chen, X. Li, A review on g-C₃N₄-based photocatalysts, *Appl. Surf. Sci.* 391 (2017) 72–123.
- [10] X. Lin, D. Xu, J. Zheng, M. Song, G. Che, Y. Wang, Y. Yang, C. Liu, L. Zhao, L. Chang, Graphitic carbon nitride quantum dots loaded on leaf-like InVO₄/BiVO₄ nanoheterostructures with enhanced visible-light photocatalytic activity, *J. Alloy. Comp.* 688 (2016) 891–898. Part B.
- [11] G. Liao, S. Chen, X. Quan, H. Yu, H. Zhao, Graphene oxide modified g-C₃N₄ hybrid with enhanced photocatalytic capability under visible light irradiation, *J. Mater. Chem.* 22 (6) (2012) 2721–2726.
- [12] G. Dong, Y. Zhang, Q. Pan, J. Qiu, A fantastic graphitic carbon nitride (g-C₃N₄) material: electronic structure, photocatalytic and photoelectronic properties, *J. Photochem. Photobiol. C Photochem. Rev.* 20 (2014) 33–50.
- [13] Wee-Jun Ong, 2D/2D graphitic carbon nitride (g-C₃N₄) heterojunction nanocomposites for photocatalysis: why does face-to-face interface matter? *Front. Mater.* 4 (11) (2017) 1–10.
- [14] Jesús Barrio, Carlos Gibaja, Jonathan Tzadikov, Menny Shalom, Félix Zamora, 2D/2D graphitic carbon nitride/antimonene heterostructure, *Struct. Char. Appl. Photocatalysis* 3 (2) (2019) 1800138.
- [15] Romero T. Bueno, Osmando F. Lopes, Kele T.G. Carvalho, Caue Ribeiro, A. Henrique, J.L. Mourão, Heterostructured semiconductors: an approach about the main challenges for obtaining and application on environmental and energy photochemical processes, *Quim. Nova* 42 (6) (2019) 661–675.
- [16] G. Mamba, A.K. Mishra, Graphitic carbon nitride (g-C₃N₄) nanocomposites: a new and exciting generation of visible light driven photocatalysts for environmental pollution remediation, *Appl. Catal. B Environ.* 198 (2016) 347–377.
- [17] G.T.S.T. Silva, K.T.G. Carvalho, O.F. Lope, C. Ribeiro, g-C₃N₄/Nb₂O₅ heterostructures tailored by sonochemical synthesis: enhanced photocatalytic performance in oxidation of emerging pollutants driven by visible radiation, *Appl. Catal. B Environ.* 216 (2017) 70–79.
- [18] R. Zhang, M. Ma, Q. Zhang, F. Dong, Y. Zhou, Multifunctional g-C₃N₄/graphene oxide wrapped sponge monoliths as highly efficient adsorbent and photocatalyst, *Appl. Catal. B Environ.* 235 (2018) 17–25.
- [19] H. Wang, L. Zhang, Z. Chen, J. Hu, S. Li, Z. Wang, J. Liu, X. Wang, Semiconductor heterojunction photocatalysts: design, construction, and photocatalytic performances, *Chem. Soc. Rev.* 43 (15) (2014) 5234–5244.
- [20] P.A. Lessing, Mixed-cation oxide powders via polymeric precursors, *Ceram. Bull.* 68 (5) (1989) 1002–1007.
- [21] L. Lutterotti, Total pattern fitting for the combined size-strain-stress-texture determination in thin film diffraction, *Nucl. Instrum. Methods Phys. Res. B* 268 (2010) 334–340.
- [22] Brian D. Vriezicke, Shane Patel, Benjamin E. Davis, Dunbar P. Birnie III, Evaluation of the Tauc method for optical absorption edge determination: ZnO thin films as a model system, *Phys. Status Solidi B* 252 (2015) 1700–1710.
- [23] Roshidah Rusdi, Azilah Abd Rahman, Nor Sabirin Mohamed, Norashikin Kamarudin, Norlida Kamarulzaman, Preparation and band gap energies of ZnO nanotubes, nanorods and spherical nanostructures, *Powder Technol.* 210 (2011) 18–22.
- [24] G.T.S.T. Silva, K.T.G. Carvalho, O.F. Lopes, E.S. Gomes, A.R. Malagutti, V. R. Mastelaro, C. Ribeiro, H.A.J.L. Mourão, Synthesis of ZnO nanoparticles assisted by N-sources and their application in the photodegradation of organic contaminants, *ChemCatChem* 9 (19) (2017) 3795–3804.
- [25] Z. Tong, D. Yang, T. Xiao, Y. Tian, Z. Jiang, Biomimetic fabrication of g-C₃N₄/TiO₂ nanosheets with enhanced photocatalytic activity toward organic pollutant degradation, *Chem. Eng. J.* 260 (2015) 117–125.
- [26] M.J. Bojdy, On New Allotropes and Nanostructures of Carbon Nitrides, Doctorate Dissertation, University of Potsdam, 2009.
- [27] J. Wang, D. Hao, J. Ye, N. Umezawa, Determination of crystal structure of graphitic carbon nitride: ab initio evolutionary search and experimental validation, *Chem. Mater.* 29 (2017) 2694–2707.
- [28] H.A.J.L. Mourão, O.F. Lopes, C. Ribeiro, V.R. Mastelaro, Rapid hydrothermal synthesis and pH-dependent photocatalysis of strontium titanate microspheres, *Mater. Sci. Semicond. Process.* 30 (2015) 651–657.
- [29] Sajid Bashir, Jingbo Liu, Hui Zhang, Xuhui Sun, Jinghua Guo, Band gap evaluations of metal-inserted titania nanomaterials, *J. Nano Res.* 15 (2013) 1572.
- [30] X.Y. Wang, Z. Liu, H. Liao, D. Klein, C. Coddet, Deoxidisation and phase analysis of plasma sprayed TiO₂ by X-ray Rietveld method, *Thin Solid Films* 473 (2005) 177–184.
- [31] S. KUMAR, S. Tonda, A. Baruah, B. Kumar, V. Shanker, Synthesis of novel and stable g-C₃N₄/N-doped SrTiO₃ hybrid nanocomposites with improved photocurrent and photocatalytic activity under visible light irradiation, *Dalton Trans.* 43 (42) (2014) 16105–16114.
- [32] D.L. Pavia, G.M. Lampman, G.S. Kriz, J.R. Vyvyan, *Introdução à espectroscopia*, Cengage Learning, 2010.
- [33] T. Setinc, M. Spreitzer, D. Vengust, I. Jerman, D. Suvorov, Inherent defects in sol-precipitation/hydrothermally derived SrTiO₃ nanopowders, *Ceram. Int.* 39 (2013) 6727–6734.
- [34] F.A. Rabuffetti, P.C. Stair, K.R. Poeppelmeier, Synthesis-Dependent surface acidity and structure of SrTiO₃ nanoparticles, *J. Phys. Chem. C* 114 (2010) 11056–11067.
- [35] B. Jurgens, E. Irran, J. Senker, P. Kroll, H. Muller, W. Schnick, Melem (2,5,8-triamino-tri-s-triazine), an important intermediate during condensation of melamine rings to graphitic carbon nitride: synthesis, structure determination by X-ray powder diffractometry, solid-state NMR, and theoretical studies, *J. Am. Chem. Soc.* 125 (2003) 10288–10300.
- [36] K.J. Kim, D.W. Moon, C.J. Park, D. Simons, G. Gillen, H. Jin, H.J. Kang, *Surf. Interface Anal.* 39 (2007) 665–673.
- [37] A.P. Dementjev, A. de Graaf, M.C.M. van de Sanden, K.I. Maslakov, A.V. Naumkin, A.A. Serov, X-ray photoelectron spectroscopy reference data for identification of the C₃N₄ phase in carbon-nitrogen films, *Diam. Relat. Mater.* 9 (2000) 1904–1907.
- [38] G.E. Muilenberg (Ed.), *Handbook of X-Ray Photoelectron Spectroscopy*, Perkin-Elmer Corporation, Eden Prairie, 1979.
- [39] N. Hellgren, R.T. Haasch, S. Schmidt, L. Hultman, I. Petrov, Interpretation of X-ray photoelectron spectra of carbon-nitride thin films: new insights from in situ XPS, *Carbon* 108 (2016) 242–252.
- [40] J.R. Pels, F. Kapteijn, J.A. Moulijn, Q. Zhu, K.M. Thomas, Evolution of nitrogen functionalities in carbonaceous materials during pyrolysis, *Carbon* 33 (11) (1995) 1641–1653.
- [41] Li Zhu, Kunkun Guo, Xuli Chen, Controllable synthesis of nitrogen-doped mesoporous carbons for supercapacitor applications, *RSC Adv.* 7 (2017) 30521–30532.
- [42] S. Biniak, G. Szymanski, J. Siedlewski, A. Swiatkowski, The characterization of activated carbons with oxygen and nitrogen surface groups, *Carbon* 35 (12) (1997) 1799–1810.
- [43] J.B. Goodenough, Electronic and ionic transport properties and other physical aspects of perovskites, *Rep. Prog. Phys.* 67 (2004) 1915–1993.
- [44] X. Pan, M.-Q. Yang, X. Fu, N. Zhang, Y.-J. Xu, Defective TiO₂ with oxygen vacancies: synthesis, properties and photocatalytic applications, *Nanoscale* 5 (2013) 3601–3614.
- [45] Y. Zheng, L. Zheng, Y. Zhan, X. Lin, Q. Zheng, K. Wei, Ag/ZnO heterostructure nanocrystals: synthesis, characterization, and photocatalysis, *Inorg. Chem.* 46 (2007) 6980–6986.